Simulation and measurement of the interplay between electron cooling, impedance, intrabeam scattering, and space charge for coasting beams

N. Biancacci[1] and M. Zampetakis[1,2]
[1]*CERN, 1211 Geneva 23, Switzerland*
[2]*Department of Physics, University of Crete, P.O. Box 2208, GR-71003 Heraklion, Greece*

(Received 24 October 2023; accepted 11 January 2024; published 30 January 2024)

The Low Energy Ion Ring (LEIR) at CERN is the first synchrotron in the Large Hadron Collider ions injector chain. The performance of LEIR is mainly determined by the number of charges extracted from the machine and transferred to the downstream chain of accelerators. Ions are delivered by the linear accelerator Linac 3. In the intensity accumulation phase, the machine operates with coasting beams: each injected beam is cooled, reducing its transverse dimensions and momentum spread, and brought into a stacking momentum position to allow subsequent injections. In this context, the evolution of the beam parameters for an injected beam under the effects of electron cooling, impedance, intrabeam scattering (IBS), and space charge is of interest in order to optimize the machine working point with respect to the accumulated intensity and to contribute to the understanding of the interplay of the different collective effects. This work describes the advancement in modeling coasting beam dynamics for LEIR accounting for the interplay of electron cooling, impedance, IBS, and space charge. Each effect is presented and progressively included to compute the simulated equilibrium longitudinal Schottky spectrum, which is found in good agreement with the measured one.

DOI: 10.1103/PhysRevAccelBeams.27.014201

I. INTRODUCTION

In the context of the general advancement in Low Energy Ion Ring (LEIR) beam dynamics modeling, accurate numerical simulations of the machine injection and accumulation process have been started. The injection process is based on the longitudinal and transverse stacking of the Linac 3 incoming beam into LEIR longitudinal and transverse acceptance [1]. The Linac 3 beam is ramped in energy in order to match the increasing energy offset of the incoming beam with respect to the circulating beam in the dispersive injection region. This mechanism enables phase space painting in the longitudinal plane while minimizing the amplitude of the betatronic oscillations of the injected beam around the closed orbit. The process is inherently dependent on the LEIR/Linac 3 energy matching, the Linac 3 transverse beam size and energy spread, and the position of the injection bump and the closed orbit with respect to the injection septum. Along this line, a new tracking tool was developed to quantitatively study the dependence of the injection efficiency on the aforementioned effects allowing to define clear tolerances against Linac 3 energy deviations and/or stray magnetic field disturbances along the injection line to LEIR [2].

While the injection process is relatively immune from collective effects (mainly due to the large momentum spread, beam sizes, and low intensity of the injected beam), this is not the case for the accumulation process: the injected beam is cooled until equilibrium is reached and brought off-momentum to allow the stacking of another injection. The electron cooler reduces transverse beam size and momentum spread, enhancing collective effects, such as impedance, intrabeam scattering (IBS), and space charge. Therefore, the complete description of this very dynamic process relies on the accurate modeling of each of these effects.

In particle accelerators, the Schottky spectrum (or power density spectrum) gathers the information from the statistical fluctuations of the beam position measured at a Schottky pickup (e.g., stripline pickups). In the absence of collective effects, and for coasting beams, the longitudinal Schottky spectrum reproduces the momentum spread distribution of the beam at each multiple of the revolution frequency f_0. Under the effect of electron cooling and longitudinal impedance, a double-peaked structure appears [3–5]. This structure is typically observed in LEIR, where operation relies on the onset of this phenomenon to steer and optimize the electron cooling process, and to allow the efficient accumulation of the Pb_{208}^{54+} ion beam intensity [1,6].

In our work, we will progressively show the simulated equilibrium longitudinal Schottky spectrum under each of

Published by the American Physical Society under the terms of the Creative Commons Attribution 4.0 International license. Further distribution of this work must maintain attribution to the author(s) and the published article's title, journal citation, and DOI.

the collective effects under study, with the aim of benchmarking the model to the measured spectrum in LEIR.

In Sec. II, we will describe the tracking code developed to model the cooling process of LEIR accounting for beam transport through the machine's optical elements, electron cooling, impedance, IBS, and space charge. The Schottky spectrum deformation is studied in the presence of these effects. In Sec. III, we will focus on the reconstruction methods applicable to retrieve the beam properties (e.g., momentum spread and impedance). Eventually, the same reconstruction methods are applied in Sec. IV to the measured Schottky spectrum in LEIR.

A similar approach, mainly focused on the effect of impedance on the Schottky spectrum, has also been started in simulations for the case of bunched beams in the Large Hadron Collider (LHC) [7].

II. NUMERICAL SIMULATIONS

A tracking code has been developed in order to study the beam dynamics of the cooling process in LEIR. The code was developed starting from PyHEADTAIL [8], adapting it to the tracking of coasting beams, adding impedance [9], electron cooling [10], IBS [11], and space charge interactions [12]. The code features the basic linear transport of charged particles in accelerators in the longitudinal and transverse planes [13]. For a particle in a coasting beam with relative momentum deviation $\delta p/p_0$ with respect to the design total momentum p_0, the turn by turn change in longitudinal position s along the accelerator is given by

$$s_2 = s_1 - \eta \frac{\delta p}{p_0} \beta c\, T_0, \tag{1}$$

where T_0 is the revolution period, βc is the beam velocity, and η is the slippage factor. Unless differently specified, the LEIR machine and beam parameters at injection are summarized in Table I in the Appendix.

Analogously, the change in transverse position and momentum is given by the machine one turn matrix $M_{x,y}$ computed with the machine optics in the horizontal and vertical planes. For the vertical plane, for example, this is given by

$$(y_2, y_2') = M_y \cdot (y_1, y_1'), \tag{2}$$

where $y' = \mathrm{d}y/\mathrm{d}s$.

After phase space initialization, the beam is tracked, the longitudinal distribution is calculated turn by turn and stored for postprocessing. Some attention needs to be taken when fast particles exceed the circumference over one turn, or, conversely, when slow particles lag one turn behind: the position of these particles is mirrored to fall between $s = 0$ and the machine circumference C.

The longitudinal distribution $\rho(s)$ is calculated on equispaced samples for $s \in [0, C)$. The Schottky spectrum is therefore calculated with a Fourier transform of the autocorrelation signal in the longitudinal plane [14].

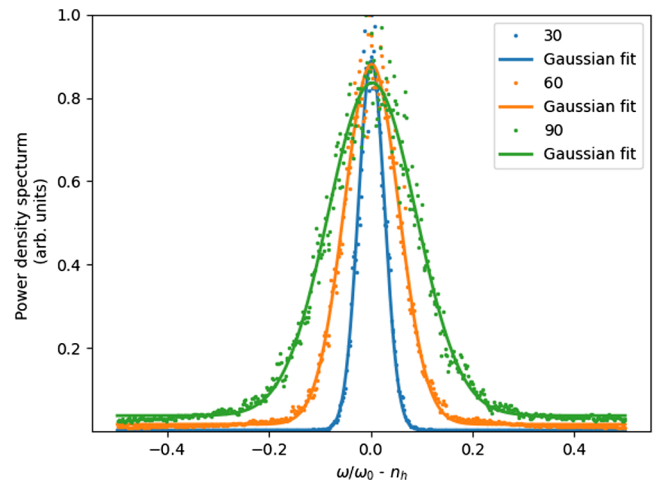

FIG. 1. Simulation of the longitudinal Schottky spectrum at three harmonics n_h (30, 60, and 90), normalized with respect to the angular frequency $\omega_0 = 2\pi f_0$. Dots refer to simulation data, lines to Gaussian fits. The momentum distribution is set to a Gaussian with standard deviation $\sigma_p = 10^{-3}$.

Figure 1 shows a tracking simulation of a beam with Gaussian momentum distribution having standard deviation $\sigma_p = 10^{-3}$. The Schottky spectrum is shown together with Gaussian fits for three harmonics n_h (30, 60, and 90), normalized with respect to the angular frequency $\omega_0 = 2\pi f_0$.

Fitting the frequency distribution at each harmonic, we can compute the rms frequency spread as shown in Fig. 2. This is compared to the theoretical one given by [14]

$$\sigma_\omega = -\eta \omega_0 \sigma_p n_h. \tag{3}$$

The agreement is satisfactory below the 60th harmonic, from which the tails of different harmonics start to overlap.

A. Electron cooling

Electron cooling is implemented with the semiempirical approach of Parkhomchuk [15]. The friction force $\mathbf{F}_{ec}$ produced by the electron beam on the ions is given by

$$\mathbf{F}_{ec} = -\frac{4 n_e m_e Z^2 r_e^2 c^4 \mathbf{V}}{(|V|^2 + V_{\mathrm{eff}}^2)^{3/2}} \log\left(\frac{\rho_{\max} + \rho_{\min} + \rho_L}{\rho_{\min} + \rho_L}\right), \tag{4}$$

where n_e is the electron beam density, m_e the electron mass, r_e the classical electron radius, Z the ion beam charge, $\mathbf{V}$ the vector of ion velocities relative to the electron beam in the three directions, and V_{eff} the effective velocity parameter related to the transverse electron beam temperature. The Coulomb logarithm is composed of three impact parameters $\rho_{\min}$, $\rho_{\max}$, and ρ_L given by

$$\rho_{\min} = Z r_e c^2 / (|V|^2 + V_s^2 + V_{\mathrm{eff}}^2), \tag{5}$$

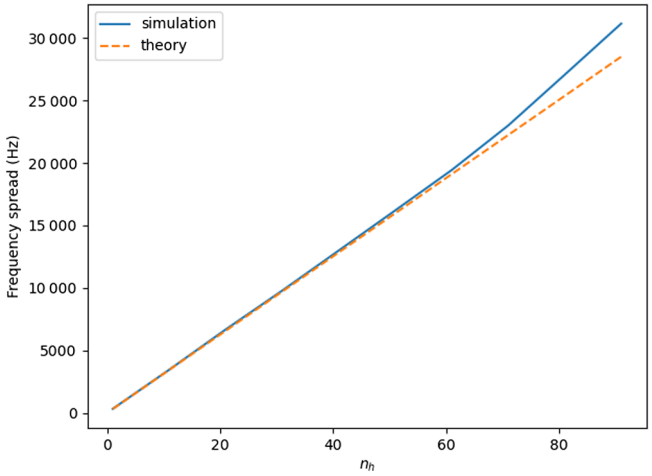

FIG. 2. Calculated frequency spread from simulation (blue solid line) and theory (orange dashed line) from harmonics 1 to 100.

$$\rho_{\max} = \frac{\sqrt{|V|^2 + V_s^2 + V_{\text{eff}}^2}}{\omega_e + 1/\tau}, \tag{6}$$

$$\rho_L = m_e V_{\text{eff}}/eB, \tag{7}$$

where V_s is an additional fitting parameter related to the longitudinal electron beam temperature [16], ω_e the electron beam plasma frequency, τ the time of flight through the cooling section, and B the guiding magnetic field.

In the following, we will consider the electron beam density $n_e = 4 \times 10^{13}$ m^{-3} and the transverse and longitudinal temperatures of approximately $k_B T_\perp = 10$ meV, and $k_B T_l = 1$ meV reported in [6] and based on direct measurements of the cooling force at LEIR. In addition, we consider the magnetic guiding field $B = 0.07$ T and the cooler length of $L_{ec} = 3$ m. The cooling force computed with these parameters is shown in Fig. 3 for the longitudinal plane. The corresponding cooling rate is $\nu \simeq 100$ s^{-1}. Considering the electron beam radius of 25 mm with uniform distribution, the electron beam current is 360 mA. Several alternative, and potentially more accurate, cooling models have been investigated in the last years [17–19] and are subject of active development (e.g., the cooling module developed for X-suite [20,21]).

B. Impedance

In particle accelerators, the impedance parameter gathers the electromagnetic interaction of the beam current with the surrounding accelerator equipment [22]. The development of a machine impedance model is performed by accounting for the impedance of each accelerator equipment in the longitudinal and transverse planes. In low energy machines, like LEIR, the impedance is largely dominated by the effect of self-fields and image charges. In the context of this work, we will limit ourselves to consider the longitudinal impedance. In LEIR, this is given by the superposition of the

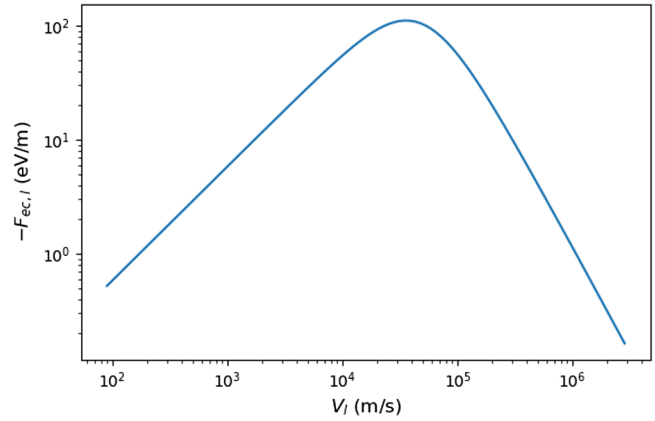

FIG. 3. Longitudinal cooling force as a function of the relative ions-electrons longitudinal velocity.

machine longitudinal impedance model and the longitudinal space charge (LSC) impedance given by [23]

$$Z_l^{\text{LSC}}(\omega)/n_h = -j\frac{Z_0}{\beta\gamma^2}\left[\frac{1}{2} + \log\left(\frac{r_{\text{pipe}}}{r_b}\right)\right], \tag{8}$$

where Z_0 is the characteristic impedance of vacuum, γ the Lorentz factor, r_b the radius of the beam transverse cross section, and $r_{\text{pipe}} = 27$ mm is the pipe aperture of the main bends [24]. Corrections for Gaussian beams of different average beam sizes $\sigma_{x,y}$ can be implemented by defining the equivalent radius $r_{b,\text{eq}} \simeq 1.747 \cdot (\sigma_x + \sigma_y)/2$ as developed in [25]. In the following, we will neglect the impedance contribution of the rest of the machine [26], which was reduced to negligible levels after the recent impedance suppression campaign [27]. A complementary overview of the effect of a machine longitudinal impedance on the longitudinal coasting beam dynamics can be found in [28].

Equation (8) establishes the connection between the longitudinal and transverse planes showing that the LSC impedance logarithmically increases during the transverse cooling process. The longitudinal momentum kick applied in the turn by turn simulations is given by [22,29,30]

$$\frac{\delta p_2}{p_0} = \frac{\delta p_1}{p_0} + W_f \cdot \mathcal{F}^{-1}(\rho(\omega) \cdot Z_l^{\text{LSC}}(\omega)), \tag{9}$$

with $\rho(\omega)$ the spectrum of the longitudinal distribution, $\mathcal{F}^{-1}$ the inverse Fourier transform, and W_f the wake factor given by

$$W_f = -\frac{Zq^2}{p_0 v}N, \tag{10}$$

with N the total number of charges in the beam, (i.e., equal to $Z \cdot N_{\text{ions}}$) and q the elementary charge. An analogous implementation is present also for the transverse impedance [12,31], although not essential for the scope of this paper.

For simplicity, and as a first step, we consider the effect of a constant impedance on a cooled beam following the

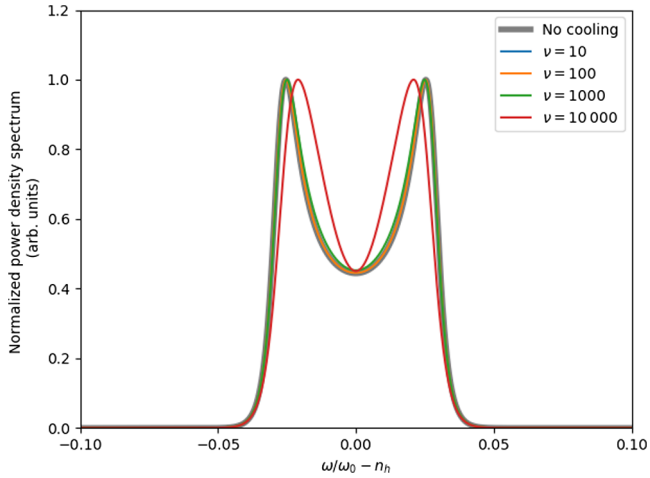

FIG. 4. Schottky spectrum as a function of the cooling rate ν in s^{-1} for a Gaussian momentum distribution with standard deviation 1.3×10^{-4}, assuming a constant impedance of $jZ_l^{\mathrm{LSC}}/n_h = 10$ kΩ and $N = 1.2 \times 10^{10}$ charges.

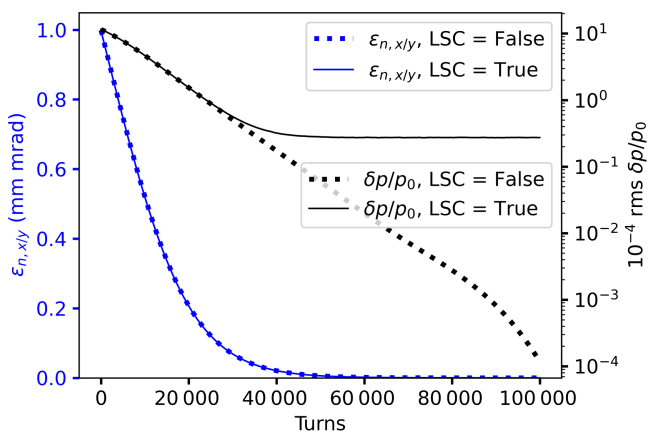

FIG. 5. Emittance and momentum evolution over the number of turns under the effect of cooling and LSC impedance: when marked true/false, the LSC impedance is included/excluded.

analytical approach of [4]. Figure 4 shows the expected longitudinal Schottky spectrum in LEIR computed with a variable cooling rate, $N = 1.2 \times 10^{10}$ charges (or 2.4×10^8 Pb_{208}^{54+} ions), in the case of a Gaussian momentum distribution with 1.3×10^{-4} standard deviation, and assuming a constant impedance $jZ_l^{\mathrm{LSC}}/n_h = 10$ kΩ.

While electron cooling is essential in order to attain a small momentum spread, the cooling rate itself has a limited effect on the Schottky spectrum, at least in the range of values achievable in LEIR. This detail will be important when discussing the reconstruction of beam properties from simulated and measured Schottky spectra in Secs. III and IV.

The case described in Fig. 4 is set up knowing the final momentum distribution, while the distribution itself, not necessarily Gaussian, is a result of the interaction between the impedance and the cooling force.

Interesting tracking simulations can already be performed limiting ourselves to the cooling and LSC impedance effects exclusively. Figure 5 shows the momentum spread evolution over 100k turns with cooling, with/without LSC impedance. The simulation assumes LEIR nominal machine parameters at injection, an initial uniform momentum distribution between $\pm 2 \times 10^{-3}$, initial normalized emittance ε_n of 1 mm mrad in the two planes, a cooling rate of 100 s^{-1} and $jZ_l^{\mathrm{LSC}}/n_h = 1$ kΩ. While cooling, the boundary for stability given by the momentum spread [4,32] reduces until Landau damping is lost. The momentum spread therefore blows up and counteracts cooling until an equilibrium is reached. On the other hand, no heating effects are included in the transverse plane, where the emittance would indefinitely reduce.

C. IBS

The IBS is limiting the cooling effect in both transverse and longitudinal planes. On the other hand, the shrinkage of the beam size also affects the longitudinal impedance through Eq. (8): as a result, the equilibrium final emittance and momentum are strongly interlinked with each other,

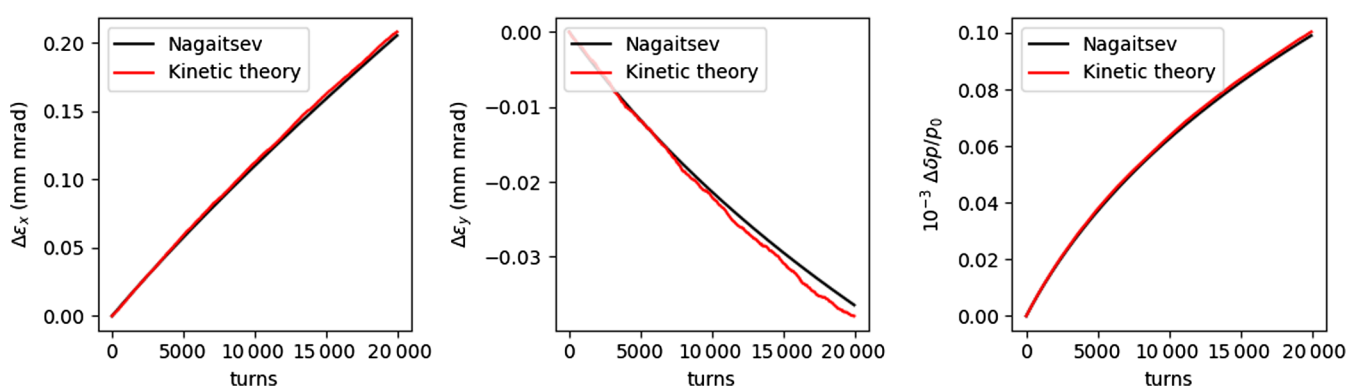

FIG. 6. Simulated evolution of horizontal and vertical emittances and momentum spread as a function of turns under the effect of IBS in LEIR. The analytical estimates from Nagaitsev's formalism are shown in black, while the results from 10 averaged tracking simulations are shown in red. The simulation assumes an initial normalized emittance of 0.2 mm mrad in the two planes, a Gaussian momentum distribution with 1×10^{-4} standard deviation, and $N = 2 \times 10^{10}$ charges.

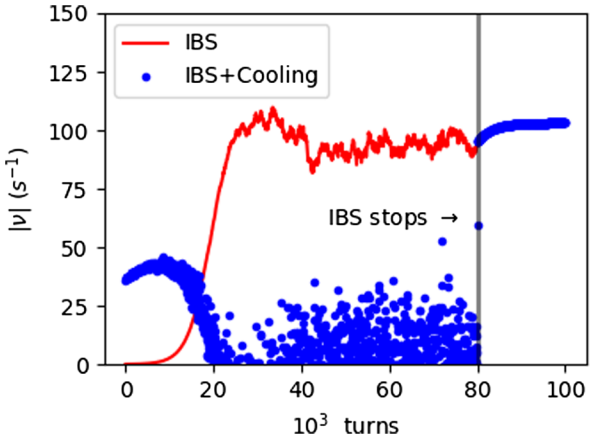

FIG. 7. Longitudinal growth rate evolution over the number of turns under the effect of cooling and IBS. The growth rate from IBS is shown in red, while the growth rate calculated from tracking simulations, i.e., including both cooling and IBS, is shown in blue. At 80k turns, the IBS is disabled and electron cooling takes over.

and numerical simulations become very helpful in studying the overall interplay.

The IBS effect was included in the simulation model based on the kinetic theory and is applied with a similar form to the Langevin equation developed and detailed in [33,34]. The IBS growth rates, given by the friction and diffusion coefficients, are evaluated using the Nagaitsev's method [35]. Every turn, each particle receives a change of its momenta depending on the beam parameters.

The emittance and momentum evolution resulting from this kick was successfully benchmarked for a bunched beam with analytical calculations using Nagaitsev's formalism for different configurations in LEIR [33]. In Fig. 6, a benchmark case for a coasting beam is shown, where the bunch length σ_b in the IBS model has been replaced with $\sigma_b = C/\sqrt{2\pi}$, where C is the machine circumference, and the longitudinal growth rate is $\nu^{\text{coasting}} = 2\nu^{\text{bunched}}$ according to [36]. A very good agreement is observed in the evolution of both horizontal and vertical emittances as well as momentum spread.

When considering the mutual effect of cooling and IBS, the equilibrium will be reached when the cooling rate ν will equal the IBS growth rate. Figure 7 shows the computed longitudinal growth rate as a function of the simulated turns in the presence of IBS and electron cooling (blue dots), together with the IBS growth rate (red line) calculated every 50 turns. To emphasize the fact that the "heating" rate from IBS matches, at equilibrium, the cooling rate from electron cooling, we disabled at 80k turns the IBS: the cooling rate, therefore, takes over and, as expected, the growth rate reached before by the IBS matches the cooling rate given by the cooling force.

When including the IBS, keeping the same simulation parameters, the evolution of Fig. 5 is substantially modified:

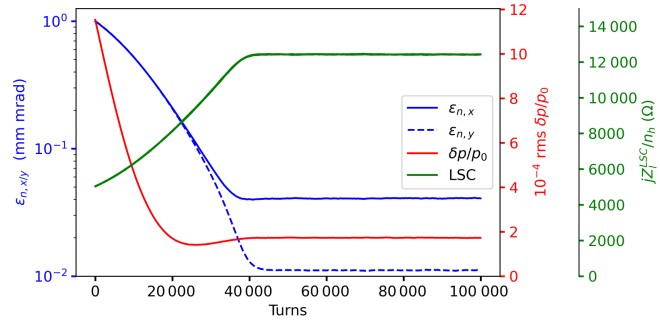

FIG. 8. Emittance and momentum evolution over the number of turns under the effect of cooling, LSC, and IBS.

on one hand, the transverse beam size does not indefinitely shrink; on the other hand, the impedance grows depending on the emittance reduction. Figure 8 shows the emittance/momentum evolution in the presence of IBS and impedance, together with the computed LSC. The cooling process reaches the equilibrium with IBS and impedance at about 40k turns. The LSC reaches $jZ_l^{\text{LSC}}/n_h \simeq 12$ kΩ.

D. Transverse space charge

The transverse space charge (TSC) plays an important role in further limiting the minimal attainable transverse emittance due to the Coulomb force repulsion. The effect is included through the implementation of the Bassetti-Erskine formula [37] used as well in other codes [38]. In the approximation of our model, no specific optics corrections in the cooler section are performed with respect to space charge. The impact on the cooling rate on the

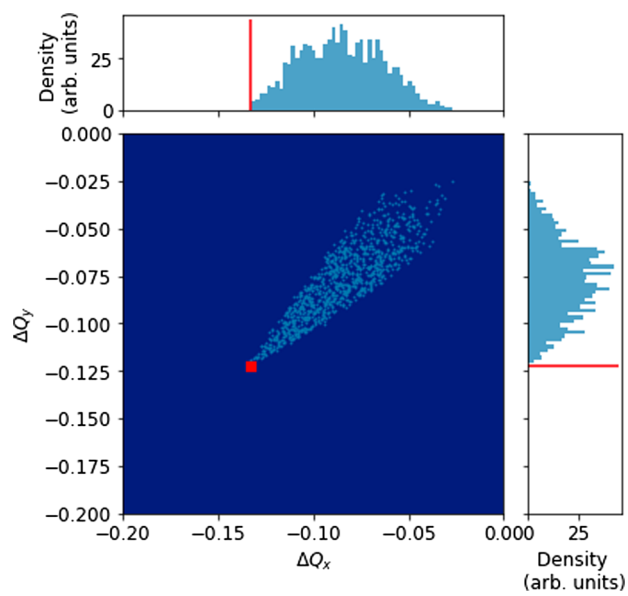

FIG. 9. Tune spread from a beam with transverse Gaussian distributions in transverse planes and momentum, together with the maximum tune shift estimated with the Laslett formula (red square). Marginal plots show the tune distribution projection in the horizontal plane (at the top) and vertical plane (at the right) together with the Laslett tune shift indicated with a red bar.

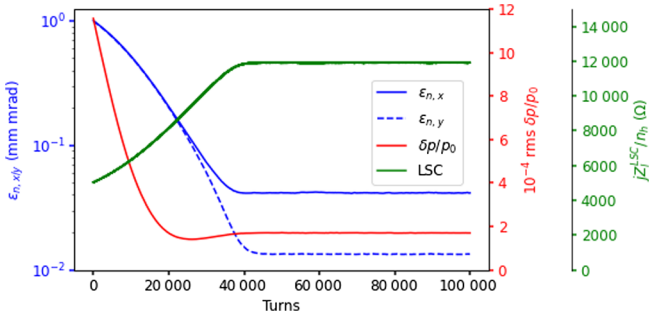

FIG. 10. Emittance and momentum evolution over number of turns under the effect of cooling, LSC, IBS, and TSC.

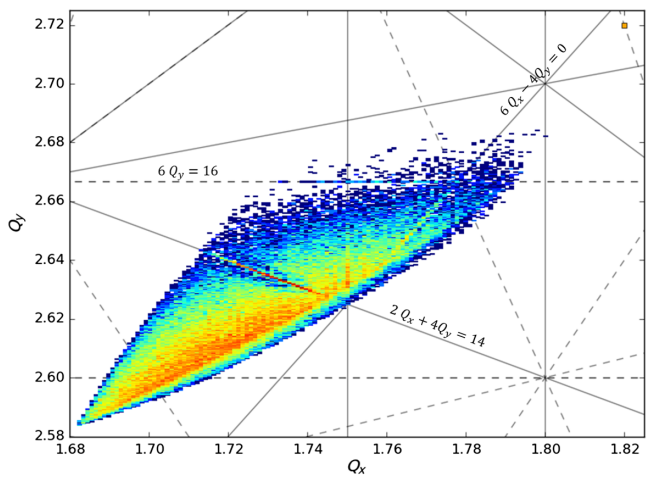

FIG. 11. Tune footprint under sole effect of nonlinear space charge resonances computed for a beam with the equilibrium parameters of Fig. 10. Normal (full lines) and skew (dashed lines) systematic resonances are shown up to 5th order. The bare machine working point is shown as an orange square.

Schottky spectrum is nevertheless expected to be negligible as shown in Fig. 4.

To correctly represent the distributed force, space charge kicks are distributed uniformly in the lattice accounting for the betatron $\beta_{x,y}(s)$ and dispersion $D_{x,y}(s)$ functions. Figure 9 shows the tune spread obtained by tracking a Gaussian coasting beam for 10k turns under transverse space charge forces. The Laslett tune shift $\Delta Q_{x,y}^{\mathrm{TSC}}$, in red, is computed analytically considering the linear approximation of the space charge force [39]

$$\Delta Q_{x,y}^{\mathrm{TSC}} = -\frac{r_p}{2\pi\beta^2\gamma^3}\frac{Z}{A}\lambda_0\int_0^C \frac{\beta_{x,y}(s)}{\sigma_{x,y}(\sigma_x+\sigma_y)}\mathrm{d}s, \tag{11}$$

with r_p the proton radius, $\lambda_0 = N/C$ the longitudinal line density, and $\sigma_{x,y}$ the beam size given by

$$\sigma_{x,y} = \sqrt{\beta_{x,y}(s)\varepsilon_{x,y} + (D_{x,y}(s)\delta p/p_0)^2}. \tag{12}$$

The space charge kicks are distributed over 30 equidistant locations along the lattice and accordingly scaled in magnitude. The beam is represented by 1×10^5 macroparticles, with intensity of 2×10^{10} charges, initial momentum spread of 1×10^{-4}, and transverse emittance of 0.5 mm mrad in the two planes. The tune footprint is computed for a subset of 1000 macroparticles and it is obtained by performing an iterative Fourier analysis [40] over the last 500 turns of betatron oscillations. The computed Laslett tune shift is found in good agreement with the maximum tune shift computed from tracking simulations.

When the transverse space charge is included in the tracking simulations, it contributes with IBS to limit the transverse beam size and counteract cooling. As we use the LEIR ideal machine lattice, only nonlinear space charge driven resonances are included in our model. Additional magnetic imperfections, like the ones related to skew sextupole errors presented in [33], are still under study and will be included in the future.

Figure 10 shows the emittance/momentum evolution under the same starting condition as the case presented in Fig. 8, while Fig. 11 shows the tune footprint computed with the equilibrium beam parameters under the sole effect

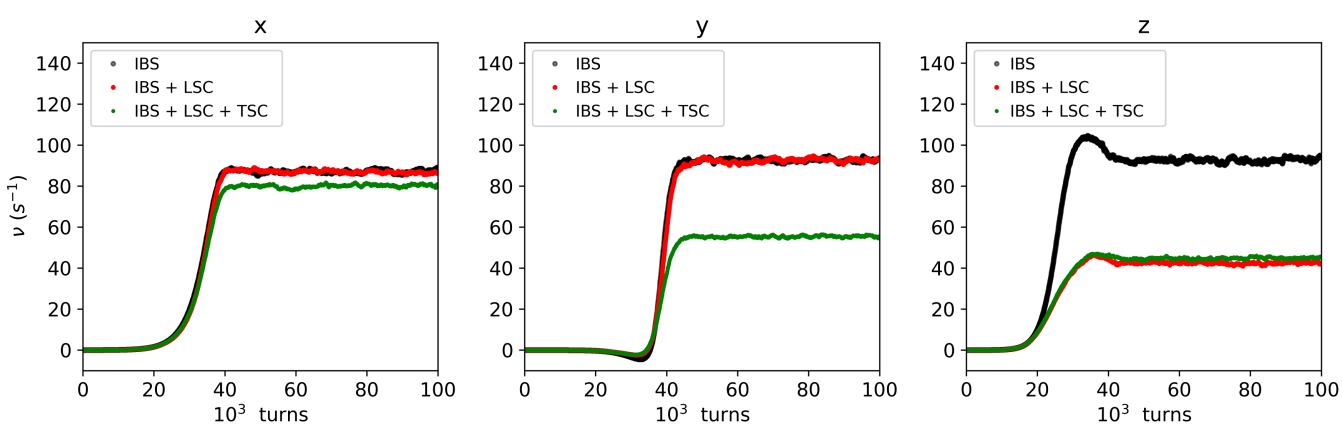

FIG. 12. IBS growth rate computed in the presence of IBS alone, IBS and LSC, and IBS, LSC, and TSC. From left to right, the growth rate over 100k turns is shown for the horizontal, vertical, and longitudinal planes.

of TSC: nonlinear space charge resonances at $6Q_y = 16$, $2Q_x + 4Q_y = 14$, and $6Q_x - 4Q_y = 0$ are mainly responsible for the TSC-related emittance growth.

Within this model, the overall equilibrium is slightly modified by the addition of the transverse space charge contribution, mainly showing a moderate increase in vertical emittance with a consequential reduction of the LSC impedance. Nevertheless, the growth rates show a sizable redistribution. In this context, Fig. 12 shows the calculated IBS growth rate in the presence of cooling, adding in step the LSC and the TSC. The longitudinal plane as expected is affected only when adding the LSC. When adding the TSC, the horizontal plane shows a slight reduction in growth rate, whereas the vertical plane is halved. This suggests that at the equilibrium, i.e., when counteracting the cooling rate from the electron cooler, in the vertical plane, the TSC and IBS contribute equally. Similarly happens in the longitudinal plane: the IBS and LSC contribute equally to match the longitudinal cooling rate. The balance is reduced in the horizontal plane, where the effect of IBS remains the dominant mechanism, as also discussed in [33].

While the longitudinal Schottky spectrum is slightly affected by TSC (we achieve similar impedance and momentum spread as in Fig. 8), this would not be the case for the transverse Schottky spectrum: a detailed study for LEIR can be found in [12], following the work of [41].

III. RECONSTRUCTION OF SIMULATED SCHOTTKY SPECTRUM

Information like momentum spread and impedance is directly available in tracking simulations but is generally more difficult to access with measurements. The simulations presented until now allow us to study the equilibrium longitudinal Schottky spectrum in the presence of cooling, LSC, IBS, and TSC. Following the work of [4], the spectrum computed in Sec. II B is used as a fitting function to reconstruct momentum spread and impedance with a least-squares minimization algorithm. As we commented in Sec. II B, the effect of the cooling rate is too small to be reliably determined through a parametric fit (at least for LEIR): it will be therefore assumed that the cooling rate is known *a priori* and equal to 100 s^{-1} in the three planes, as introduced in Sec. II A.

Fig. 13 shows the simulated longitudinal Schottky spectrum at $n_h = 100$ corresponding to the equilibrium reached in Fig. 10 at 100k turns and averaged over 20 simulations. Simulated data are shown together with the reconstruction performed either using the equilibrium momentum distribution and impedance from the simulation (direct method), or parametrically fitting the Schottky spectrum (reverse method), i.e., leaving the equilibrium momentum distribution and the impedance as free parameters to be determined. The momentum distribution is supposed to be Gaussian.

The equilibrium momentum distribution and the impedance retrieved from the reverse reconstruction are shown in

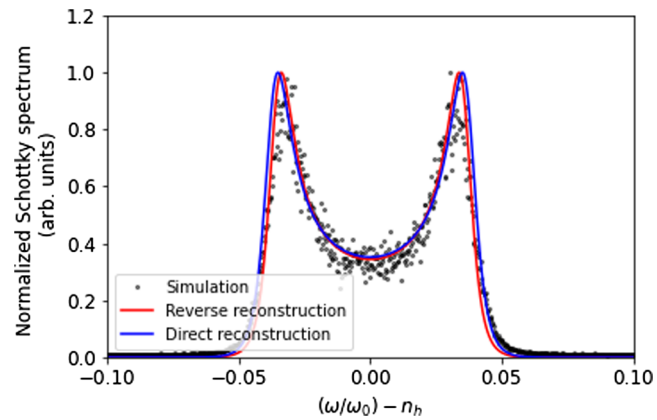

FIG. 13. Simulated Schottky spectrum at $n_h = 100$ (black dots) reconstructed with direct (blue line) and reverse methods (red line).

Fig. 14, where the algorithm is applied from $n_h = 10$ to $n_h = 100$ in steps of 10 harmonics. At the top, the reconstructed impedance is shown against the value reached at the equilibrium in the simulations: the agreement is acceptable and within 10%. The remaining discrepancy might be related to limitations in the numerical simulations or in the underneath theory: we nevertheless retain that the

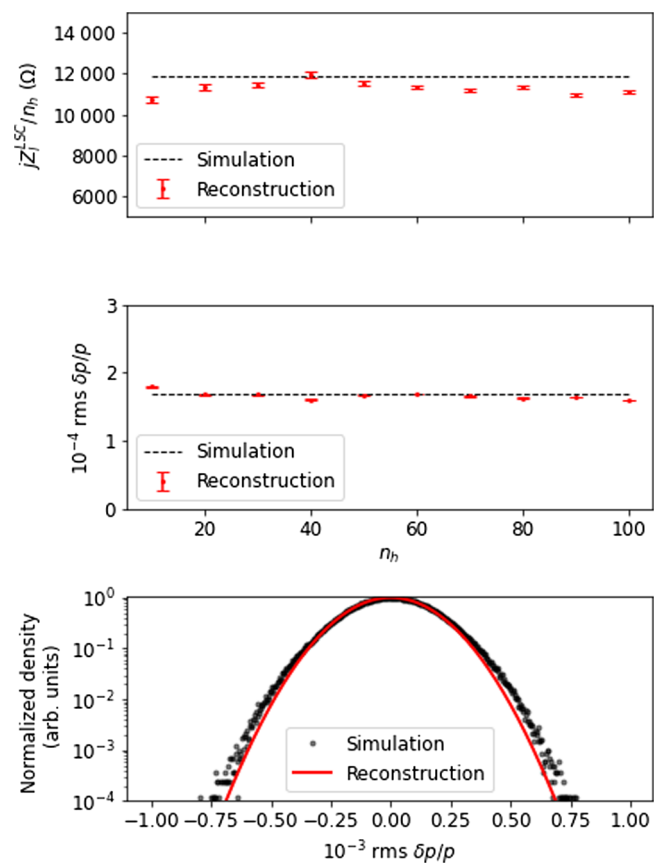

FIG. 14. Reconstruction of impedance (top), momentum spread (middle), and corresponding momentum distribution (bottom) in red, against simulated data, in black.

reached accuracy is reasonable for the target of our studies. At the center, the reconstructed momentum spread is shown, in very good agreement with the simulated one. This is also visible at the bottom, where the final momentum distribution is shown together with the reconstructed one.

IV. RECONSTRUCTION OF MEASURED SCHOTTKY SPECTRUM IN LEIR

Beam measurements were performed in LEIR in order to study the equilibrium emittance and momentum spread with the help of longitudinal Schottky measurements. A beam with intensity $N \simeq 1.5 \times 10^{10}$ charges is injected from Linac 3 and cooled at the machine flat bottom energy. The alignment with the electron cooler was determined by performing the so-called cooling maps [6], i.e., aligning the beam orbit in the cooler section to minimize the final equilibrium emittance. The overall measurement is performed over 1400 ms, i.e., over about 500k turns.

Figure 15 shows the evolution of intensity and emittance versus time. The Schottky measurements were performed once equilibrium was reached, from 1290 ms over a 50 ms window. Due to intrinsic limitations of the system, and to reduce the amount of delivered data, the spectrum was measured at a single harmonic for each measurement. Several measurements were acquired in order to improve the signal to noise ratio of the Schottky spectrum (typically 25 per measured harmonic) and span from harmonic $n_h = 10$ to 100. The beam size was measured with Ionization Profile Monitors (IPMs) in the horizontal and vertical planes [42]. The emittance is reconstructed scaling for the β function at the instruments computed with MAD-X ($\beta_x^{\mathrm{IPM}} = 15.7$ m and $\beta_y^{\mathrm{IPM}} = 5.7$ m). The LSC impedance is computed with Eq. (8) considering the average beam size along the machine (in LEIR $\bar{\beta}_x \simeq 8$ m and $\bar{\beta}_y \simeq 7$ m).

When applying the reconstruction procedure detailed in the previous section, we can retrieve the information on the impedance and momentum spread reached at the equilibrium. Figure 16 shows these parameters for the measured harmonics: the reconstruction is stably giving an impedance of about 10 kΩ, in agreement with the one calculated and shown in Fig. 15, and a momentum spread of about 1.3×10^{-4} close to the 1.6×10^{-4} simulated and shown in

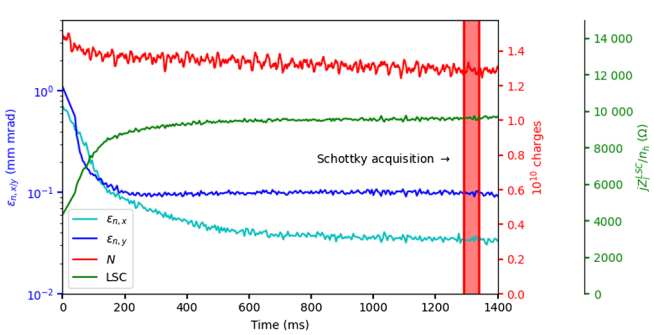

FIG. 15. LEIR cycle overview.

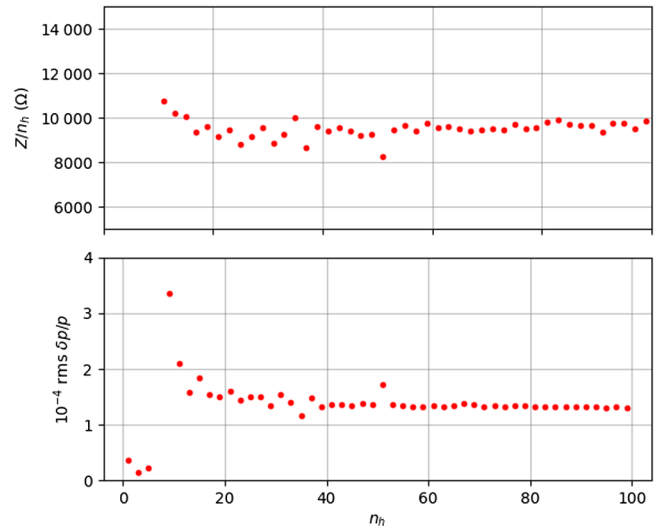

FIG. 16. Reconstruction of impedance (top) and momentum spread (bottom) from measured Schottky spectrum in LEIR.

Fig. 14. The reconstruction fit is shown in Fig. 17 together with measured data in correspondence to the harmonic $n_h = 100$. As introduced in Sec. II A, a cooling rate of 100 s^{-1} is assumed, based on the direct measurement of the cooling force at LEIR.

Comparing the results shown in Figs. 14 and 16, despite the complexity of the beam dynamics involved, we remark a very good agreement of the reconstructed momentum spread and impedance at the equilibrium. In addition, the horizontal emittance shown in Fig. 15 is in agreement with the simulated one shown in Fig. 10. The vertical emittance is, instead, showing an order of magnitude larger value, which may be related to additional heating effects not yet considered in the simulation model: for example, as commented in Sec. II D, the $3Q_y = 8$ skew resonance driven by lattice imperfections, analyzed in [33], could play a relevant role also in this context and will be investigated in the future. It is interesting to notice that the larger vertical emittance achieved in measurements is also reflected in the value of the LSC impedance: according to Eq. (8), a factor 10 larger vertical emittance translates into a

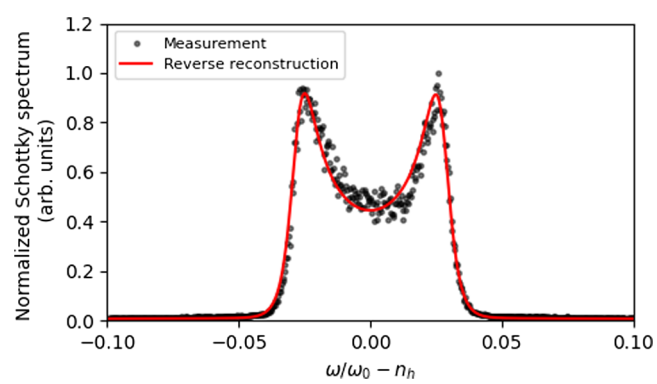

FIG. 17. Measured Schottky spectrum at $n_h = 100$ (black dots) and reconstructed with reverse method (red line). A cooling rate of 100 s^{-1} is assumed.

factor ~3 larger vertical beam size, which in turn, reduces by 15%–20% the LSC impedance due to the logarithmic dependence, as observed in the measurements.

The overall cooling time for the vertical plane is ~200 ms, i.e., ~70 k turns, close to the ~40 k turns simulated and shown in Fig. 10. The horizontal plane is cooling on a longer time scale (~600 ms). However, being the horizontal IPM in a dispersive region ($D_x^{\mathrm{IPM}} = -1$ m), this may actually reflect a longer cooling time in the longitudinal plane. In addition, also a different injection momentum distribution could have an effect on the cooling time: the Linac 3 delivers a momentum distribution that we modeled as uniform between $\pm 2 \times 10^{-3}$ in relative momentum deviation. Nevertheless, some tails can extend over the upper/lower limits, smoothing the hard edges of a uniform distribution, and lengthening the cooling time. These aspects will be the subject of future detailed investigations.

V. CONCLUSIONS

In this work, we presented the development of comprehensive simulations accounting for the interplay of electron cooling, impedance, IBS, and transverse space charge for coasting beams at injection energy in LEIR. The simulations allowed us to study the evolution of the beam properties from injection in LEIR to equilibrium while being able to disentangle the contribution of each effect separately. It is the first time that the complete cooling process is simulated in a tracking code for LEIR, accounting for the progressive onset of collective effects and their impact on the equilibrium beam parameters.

The longitudinal Schottky spectrum has been used as a benchmark tool for comparing our simulations to measurements. Direct and reverse reconstruction techniques were tested in simulations to recover the impedance and momentum spread of the beam once at equilibrium. Measurements of the longitudinal Schottky spectrum have been presented for LEIR, showing a good agreement with simulations in terms of achieved impedance and momentum spread.

While measurements and simulations are sufficiently inline in terms of reconstructed momentum spread, impedance, and equilibrium horizontal emittance, a discrepancy is present concerning the equilibrium vertical emittance. Recent work suggests that the effect of additional nonlinearities could play a role in reducing this discrepancy. In this respect, simulations including this additional heating mechanism are planned for the future. The vertical cooling time is comparable to simulations, whereas the longitudinal/horizontal appears longer and will be the subject of future dedicated measurements.

APPENDIX: LEIR PARAMETERS

In Table I, we report the main LEIR machine and beam parameters at injection energy.

TABLE I. LEIR machine and beam parameters at injection.

Parameter	Value	Description
Energy	4.2 MeV/u	Injection kinetic energy
βc	0.095 c	Beam velocity
γ	1.0045	Lorentz factor
η	−0.867	Slippage factor
α_c	0.1241	Compaction factor
Q_x	1.81	Horizontal tune
Q_y	2.72	Vertical tune
C	25π m	Circumference
T_0	2.76 μs	Revolution period
f_0	362 kHz	Revolution frequency
$\delta p/p_0$	$\pm 2 \times 10^{-3}$	Injected momentum
N	$1\text{–}2 \times 10^{10}$	Charges/injection

[1] M. Benedikt, P. Collier, V. Mertens, J. Poole, and K. Schindl, LHC Design Report: The LHC injector chain, CERN, Geneva, Switzerland, Report No. CERN-2004-003-V-3, 2004.

[2] N. Biancacci, R. Alemany Fernandez, G. Bellodi, D. Bodart, M. Bozzolan *et al.*, Advancements in injection efficiency modelling for the Low Energy Ion Ring (LEIR) at CERN, in *Proceedings of 14th International Particle Accelerator Conference, IPAC-2023, Venice, Italy* (JACoW, CERN, Geneva, Switzerland, 2023).

[3] S. Chattopadhyay, Some fundamental aspects of fluctuations and coherence in charged-particle beams in storage rings, CERN, Geneva, Switzerland, Technical Report No. CERN-YELLOW-84-11, 1984.

[4] S. Cocher and I. Hofmann, On the stability and diagnostics of heavy ions in storage rings with high phase space density, Part. Accel., **34**, 189 (1990), https://inspirehep.net/literature/280339.

[5] V. Ziemann, Analytic expressions for longitudinal Schottky signals from beams with Gaussian momentum distribution, in *Proceedings of 17th Particle Accelerator Conference, Vancouver, Canada* (IEEE, New York, 1997).

[6] S. Albright, R. Alemany Fernandez, M. E. Angoletta, H. Bartosik, N. Biancacci *et al.*, Review of LEIR operation in 2018, CERN, Geneva, Switzerland, Technical Note No. CERN-ACC-Note-2020-0023, 2019.

[7] C. Lannoy, D. Alves, K. Łasocha, N. Mounet, and T. Pieloni, LHC Schottky spectrum from macro-particle simulations, in *Proceedings of the 11th International Beam Instrumentation Conference, IBIC 2022, Kraków, Poland* (JACoW, Geneva, Switzerland, 2022), pp. 308–312.

[8] PyHEADTAIL, https://github.com/PyCOMPLETE/.

[9] N. Biancacci, pyHEADTAIL for coasting beams, in *Proceedings of the 178th HSC Section Meeting* (CERN, Geneva, Switzerland, 2019).

[10] N. Biancacci and A. Latina, Status of longitudinal electron cooling simulations with RF-track and PyHeadtail, in *Proceedings of LIU-Ions PS injectors Performance Coordination Meeting* (CERN, Geneva, Switzerland, 2020).

[11] N. Biancacci and M. Zampetakis, IBS and electron cooling simulations for LEIR, in *Proceedings of the Ions MPC Meeting* (CERN, Geneva, Switzerland, 2022).
[12] N. Biancacci, Interpretation of the LEIR Schottky spectra, in *Proceedings of the CEI Meeting* (CERN, Geneva, Switzerland, 2022).
[13] S. Y. Lee, *Accelerator Physics* (World Scientific, Singapore, 2011), 3rd ed.
[14] F. Caspers, Schottky signals for longitudinal and transverse bunched-beam diagnostics, in *Proceedings of the CAS-CERN Accelerator School: Beam Diagnostics, Dourdan, France* (CERN, Geneva, Switzerland, 2008).
[15] V. V. Parkhomchuk, New insights in the theory of electron cooling, Nucl. Instrum. Methods Phys. Res., Sect. A **441**, 9 (2000).
[16] H. Nersisyan, C. Toepffer, and G. Zwicknagel, *Interactions Between Charged Particles in a Magnetic Field: A Theoretical Approach to Ion Stopping in Magnetized Plasmas* (Springer, Berlin, 2007).
[17] A. Latina, H. Bartosik, N. Biancacci, R. Corsini, D. Gamba *et al.*, Electron cooling simulation and experimental benchmarks at LEIR, in *Proceddings of 9th International Particle Accelerator Conference, Vancouver, BC, Canada, IPAC-2018* (JACoW, CERN, Geneva, Switzerland, 2018), TUPAF039.
[18] B. Veglia, N. Biancacci, D. Gamba, A. Latina, J. Resta-López *et al.*, Electron cooling simulation benchmarking, in *Proceedings of 12th Workshop on Beam Cooling and Related Topics, COOL-2019, Novosibirsk, Russia* (JACoW, CERN, Geneva, Switzerland, 2019), TUPS06.
[19] A. Borucka, D. Gamba, and A. Latina, Comparison of available models of electron cooling and their implementations, in *Proceedings of 13th Workshop on Beam Cooling and Related Topics, COOL-2021, Novosibirsk, Russia*, (JACoW, CERN, Geneva, Switzerland, 2021), pp. 74–77.
[20] P. Kruyt, D. Gamba, and G. Franchetti, Advancements and applications of cooling simulation tools: A focus on X-suite, in *Proceedings of the COOL 2023 Conference, Montreux, Switzerland* (CERN, Geneva, 2023).
[21] X-suite, https://github.com/xsuite.
[22] L. Palumbo, V. G. Vaccaro, and M. Zobov, Wake fields and impedance, CAS Advanced School on Accelerator Physics, Rhodes, Greece, Report No. LNF-94-041-P, 1994.
[23] R. L. Gluckstern, Analytic methods for calculating coupling impedances, CERN Yellow Reports: Monographs, CERN, Geneva, Switzerland, Report No. CERN-2000-011, 2000.
[24] N. Biancacci, H. Bartosik, M. Gasior, S. Hirlaender, A. Latina *et al.*, Impedance and instability studies in LEIR with xenon, in *Proceedings of the 9th International Particle Accelerator Conference, IPAC-2018, Vancouver, BC, Canada* (JACoW, CERN, Geneva, Switzerland, 2018).
[25] M. Venturini, Models of longitudinal space-charge impedance for microbunching instability, Phys. Rev. ST Accel. Beams, **11**, 034401 (2008).
[26] LEIR impedance, http://impedance.web.cern.ch (2020).
[27] N. Biancacci, R. Alemany Fernandez, Y. Alexahin, M. Carlà, J. Eldred *et al.*, Impedance localization and identification, in *Proceedings of the ICFA Mini-Workshop on Mitigation of Coherent Beam Instabilities in Particle Accelerators, MCBI-2019, Zermatt, Switzerland* (CERN, Geneva, Switzerland, 2019).
[28] J. L. Laclare, Coasting beam longitudinal coherent instabilities, in *Proceedings of the CAS-CERN Accelerator School: 5th General Accelerator Physics Course* (CERN, Geneva, Switzerland, 1994), pp. 349–384.
[29] A. W. Chao, *Physics of Collective Beam Instabilities in High Energy Accelerators* (John Wiley & Sons, Inc., New York, 1993).
[30] K. Y. Ng, *Physics of Intensity Dependent Beam Instabilities* (World Scientific, Hoboken, NJ, 2006).
[31] N. Biancacci, E. Métral, and M. Migliorati, Fast-slow mode coupling instability for coasting beams in the presence of detuning impedance, Phys. Rev. Accel. Beams **23**, 124402 (2020).
[32] K. Hubner and V. G. Vaccaro, Dispersion relations and stability of coasting particle beams, CERN, Geneva, Switzerland, Technical Report No. CERN-ISR-TH-70-44, 1970.
[33] M. Zampetakis, F. Antoniou, F. Asvesta, H. Bartosik, and Y Papaphilippou, Interplay of space charge and intra-beam scattering in the LHC ion injector chain, arXiv:2310.03504.
[34] M. Zampetakis, F. Antoniou, H. Bartosik, and Y. Papaphilippou, Interplay of space charge, intra-beam scattering and synchrotron radiation in the CLIC damping rings, arXiv:2308.02196.
[35] S. Nagaitsev, Intrabeam scattering formulas for fast numerical evaluation, Phys. Rev. ST Accel. Beams **8**, 064403 (2005).
[36] A. Piwinski, Intra-beam-scattering, in *Proceedings of the 9th International Conference on High-Energy Accelerators, Stanford, CA, 1974* (Stanford Linear Accelerator Center, Stanford University, CA, 1974), pp. 405–409.
[37] M. Bassetti and G. A. Erskine, Closed expression for the electrical field of a two-dimensional Gaussian charge, CERN, Geneva, Switzerland, Technical Report No. CERN-ISR-TH-80-06, 1980.
[38] A. Oeftiger and S. E. Hegglin, Space charge modules for PyHEADTAIL, in *Proceedings of the HB2016, Malmö, Sweden* (CERN, Geneva, Switzerland, 2016).
[39] K. Schindl, Space charge, in *Proceedings of the CAS-CERN Accelerator School: Intermediate Course on Accelerator Physics, Zeuthen, Germany* (CERN, Geneva, Switzerland, 2003).
[40] R. Bartolini and F. Schmidt, A computer code for frequency analysis of non-linear Betatron motion, CERN, Geneva, Switzerland, Technical Report No. SL-Note-98-017-AP, 1998.
[41] S. Paret, V. Kornilov, O. Boine-Frankenheim, and T. Weiland, Transverse Schottky and beam transfer function measurements in space charge affected coasting ion beams, Phys. Rev. ST Accel. Beams **13**, 022802 (2010).
[42] C. Bal, V. Prieto, R. Sautier, and G. Tranquille, First results from the LEIR ionisation profile monitors, in *Proceedings of the 8th European Workshop on Beam Diagnostics and Instrumentation for Particle Accelerators, DIPAC-2007, Venice, Italy* (CERN, Geneva, Switzerland, 2008).